IOP Publishing Journal of Physics D: Applied Physics
J. Phys. D: Appl. Phys. **47** (2014) 125203 (12pp) doi:10.1088/0022-3727/47/12/125203

Stabilization of boundary layer streaks by plasma actuators

Mark Riherd and Subrata Roy

Applied Physics Research Group, University of Florida, Gainesville, FL 32611, USA

E-mail: roy@ufl.edu

Received 19 October 2013, revised 31 December 2013
Accepted for publication 27 January 2014
Published 6 March 2014

Abstract

A flow's transition from laminar to turbulent leads to increased levels of skin friction. In recent years, dielectric barrier discharge actuators have been shown to be able to delay the onset of turbulence in boundary layers. While the laminar to turbulent transition process can be initiated by several different instability mechanisms, so far, only stabilization of the Tollmien–Schlichting path to transition has received significant attention, leaving the stabilization of other transition paths using these actuators less explored. To fill that void, a bi-global stability analysis is used here to examine the stabilization of boundary layer streaks in a laminar boundary layer. These streaks, which are important to both transient and by-pass instability mechanisms, are damped by the addition of a flow-wise oriented plasma body force to the boundary layer. Depending on the magnitude of the plasma actuation, this damping can be up to 25% of the perturbation's kinetic energy. The damping mechanism appears to be due to highly localized effects in the immediate vicinity of the body force, and when examined using a linearized Reynolds-averaged Navier–Stokes energy balance, indicate negative production of the perturbation's kinetic energy. Parametric studies of the stabilization have also been performed, varying the magnitude of the plasma actuator's body force and the spanwise wavenumber of the actuation. Based on these parametric studies, the damping of the boundary layer streaks appears to be linear with respect to the total amount of body force applied to the flow.

Keywords: plasma actuation, TS wave, boundary layer streaks, bi-global stability

(Some figures may appear in colour only in the online journal)

1. Introduction

The control of the laminar to turbulent transition process in boundary layers is one that is of utmost importance in reducing the drag experienced by air and ground vehicles. The benefits of drag reduction are both economic and environmental, as reduced drag leads to reduced fuel consumption, reducing the operation cost of these vehicles and their impact on the environment. Delaying the onset of turbulence in a boundary layer reduces the extent of the vehicle wetted by a turbulent, high drag flow, and increases the amount of the vehicle wetted by a laminar, low drag flow. As such, so long as the flow remains attached, the viscous drag can be reduced by forcing the flow to remain laminar.

In recent years, attention to the use of dielectric barrier discharge (DBD) actuators for transition control purposes has increased. DBD actuators are plasma devices that can be used to generate a localized electro-hydrodynamic body force (EHD), which can then be used to modify the surrounding flow field. These devices have been reviewed with regard to their fundamental physics [1] and their applications [2, 3]. The benefits of these actuators include low power consumption, surface compliance, rapid response (due to their lack of moving parts), and high bandwidth, but these benefits come with the challenges of limited control authority compared to other types of flow control actuators. Grundmann and Tropea showed that plasma actuators could be used to delay the onset of turbulence in a laminar boundary layer [4, 5]. A number of studies followed by various researchers, and the focus for many of these studies remained on the Tollmien–Schlichting (TS) route to turbulence [4, 6–10].

While stabilizing the TS transition path is useful, it is not the only transition mechanism in boundary layers known to exist [11]. Stabilizing this one mechanism does not necessarily

 © 2014 IOP Publishing Ltd Printed in the UK

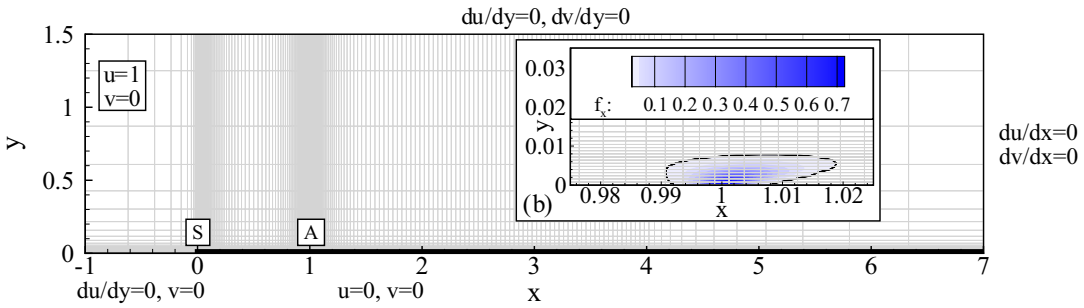

Figure 1. (*a*) The two-dimensional domain and boundary conditions used for the baseline flow modifications, and (*b*) a close up of the co-flow oriented body force used within the boundary layer. Every fourth grid point is shown. From Riherd and Roy [10].

imply that all of the remaining paths to turbulence are also stabilized. The transient growth of boundary layer streaks and transition due to free stream turbulence (two growth mechanisms thought to be related to each other [12–15]) are areas where the use of plasma actuation for stabilization is still largely unknown. Only limited research has been completed with the goal of using DBD actuators to stabilize boundary layer streaks, but that work has been primarily concerned with developing a system to actively cancel the streaks using streamwise oriented actuators [16, 17].

In terms of hydrodynamic stability, boundary layer streaks present an array of complex behaviour. Fransson and his co-workers demonstrated that these streaks can be used to stabilize boundary layer flows against other instabilities when they are introduced in a controlled manner to the flow [18, 19]. However, other researchers have shown that once these streaks become sufficiently large in magnitude, the resulting flows are subject to exponential [20] and algebraic [21] instabilities of their own, leading to the onset of turbulence in the flow. The difference in behaviours indicates the potential for boundary layer streaks to be stabilizing or destabilizing, depending on the circumstances of the flow. With the goal of flow stabilization in mind, the most prudent approach to managing boundary layer streaks may be to limit their growth such that they remain small enough in magnitude so that they do not become unstable.

The present work focuses on the passive (open loop) control of boundary layer streaks using plasma actuators, but the control of the transition process has been considered using a number of different non-plasma methods. The use of distributed roughness elements [18, 19], boundary layer suction [22, 23], riblets [24, 25], and other methods have been examined. A unifying feature between all of these methods is that they modify the base flow and its stability properties, though in different ways. Plasma actuators have certain advantages over these other approaches, as they are surface compliant can be turned off (unlike roughness elements or riblets) and do not require extensive pumping and piping systems (unlike suction). However, the high voltages required to power plasma actuators does present itself as a challenge, though not as one that is insurmountable.

The present study focuses on the use of DBD plasma actuators to reduce the magnitude of boundary layer streaks in a passive manner as part of a broader goal of stabilizing boundary layer flows against the wider spectrum of exponential, algebraic, and by-pass paths to turbulence. This paper is organized as follows. In section 2, baseflows implementing plasma actuators are simulated. In section 3, a numerical method is outlined by which the stability of these base flows will be characterized. Section 4 presents relevant results and describes how the stability of these flows is modified by the addition of plasma actuation. Finally, a brief summary concluding these results is presented in section 5.

2. Determination of the base flow

All types of linear stability analysis require a base flow to examine. As a starting point to examine the effects of plasma-based momentum addition on a zero pressure gradient boundary layer, this flow has been simulated numerically. In order to be consistent with previous studies, base flows from Riherd and Roy [10] are used for this work as well. These simulations were done using a Navier–Stokes solver, FDL3DI [26], which solves the compressible, diagonalized form of the Navier–Stokes equations. Incompressible flows can be simulated by setting the Mach number to an appropriately low value. Using a Mach number of $M_\infty = 0.1$ in the simulations, the maximum variations to the fluid density are found to be on the order of 0.15% throughout the domain, indicating that the flow is essentially incompressible. Temperature (and viscosity via Sutherland's law) variations are found to be similarly small, hence, an incompressible assumptions should be sufficient for the flow stability analysis.

A fine, two-dimensional mesh (801 × 151) is used as a domain for the simulation. This domain is non-dimensionalized by the length (L) from the leading edge of the plate (S in figure 1(*a*)) to the actuator location (A in figure 1(*a*)). The domain extends from one unit of length (L) upstream of the leading edge to seven units of length (7L) downstream of the leading edge location. This mesh resolves the near wall boundary layer, effects near a sharp leading edge (but not the leading edge itself), and the steady addition of momentum through a body force term. Farther away from the actuator, the mesh is coarsened in order to prevent unsteady effects from reflecting off of the boundary conditions. At the location of the plasma actuator (A, $x = 1$, $Re_x = \frac{u_\infty x}{\nu} = 100\,000$), 62 points are used to resolve the boundary layer height ($\delta_{99\%} = 0.0158$). 45 points are used to resolve the body force in the streamwise direction and 43 points are used to resolve the body force in the wall normal direction. This mesh is adequate for resolving the flow details near regions of high gradients, and

Table 1. Dimensional and non-dimensional values used to compute the base flow.

Reference Parameter	Value
Dimensional values	
u_∞	$7.5\,\mathrm{m\,s^{-1}}$
L	$0.20\,\mathrm{m}$
ρ_∞	$1.20\,\mathrm{kg\,m^{-3}}$
ν	$1.5 \times 10^{-5}\,\mathrm{m^2\,s^{-1}}$
Non-dimensional values	
Re	100 000
Pr	0.72
Ma	0.1
D_c	varies, see figure 2(*a*)

these simulations should be considered a direct numerical simulation. A schematic of the domain is shown in figure 1. A summary of the dimensional and non-dimensional parameters used for this study are given in table 1.

The plasma actuation is modelled using an approximate body force distribution based on first principles simulations of the plasma discharge [27] (figure 1(*b*)) in a manner consistent with the description in Rizzetta *et al* [26]. A more rigorous multi-scale analysis may capture the physics of the plasma better, but it is anticipated that its response to the flow will not be greatly affected by this approximation or the very high frequency unsteady behaviour ($\mathcal{O}(10\,\mathrm{kHz})$, $F \times 10^6 = \frac{2\pi f}{u_\infty^2} \times 10^6 = \mathcal{O}(10^4)$) normally damped out by the boundary layer. Importantly, such an approximation alleviates the expensive computational requirements of a coupled fluid-plasma simulation. The magnitude of the plasma actuation, however, is modulated through a non-dimensional parameter, D_c, which relates the magnitude of the body force to the dynamic pressure (i.e. $D_c = \frac{|f_0|L}{\rho u_\infty^2}$).

Instead of defining the magnitude of the body force through a characteristic force density, the magnitude of the body force is characterized by how strong of a wall jet it can generate under quiescent conditions, which was determined before simulations of the plasma actuator in a boundary layer. The same set up was used with no slip conditions ($u = v = 0$) for the left, right, and bottom boundaries, with a no shear condition on the upper boundary, leading to a quiescent condition over a majority of the domain. The body force distribution was operated at various values of D_c with quiescent initial conditions, representing an increase in the operating voltage of the plasma actuator. As the body force distribution is kept constant for all of the simulations performed as part of this study, the value of D_c is directly proportional to the amount of total amount of body force used to inject momentum into the flow. The effect of the actuation on the flow is characterized by the maximum velocity induced in the resulting wall jet (u_p, shown in figure 2). An interpolation was then used to control the body force for the simulation under non-quiescent conditions. The magnitude of the implemented force is characterized by the non-dimensional parameter

$$\gamma_0 = \frac{u_p\big|_{x_0,\mathrm{quiescent}}}{u_\infty}. \tag{1}$$

This parameter is selected in order to focus on the fluid dynamic effect of the plasma actuation and its influence on the flow stability, neglecting the electrical inputs such as voltage, frequency and the waveform driving the device. The values of γ_0 are calibrated for the Reynolds number tested as part of this study.

Putting this body force into more tangible terms, the total streamwise oriented body force introduced by this distributed force model is 2.53×10^{-5} in non-dimensional terms. Using the dimensional parameters laid out in table 1, the total dimensional force per unit width provided to the flow is equal to $0.342 \times D_c\,\mathrm{mN\,m^{-1}}$. For the case of $\gamma_0 = 0.25$, $D_c = 12.87$, which results in a total force of $4.40\,\mathrm{mN\,m^{-1}}$, which is reasonable for generating a $1.88\,\mathrm{m\,s^{-1}}$ wall jet when compared to experimental results [28].

In these simulations, the body force was placed at a position corresponding to $\mathrm{Re}_x = 100\,000$ ($Re_{\delta^*} = \frac{u_\infty \delta^*}{\nu} = 543$, where $\delta^* = \int_0^\infty (1 - \frac{u}{u_\infty})\mathrm{d}y$) in a boundary layer flow. This actuator location is in the transitional regime, which is useful for understanding how the momentum addition modifies the laminar to turbulent transition in the critical domain.

In examining the flow fields around the plasma actuator, the addition of momentum shows a local impact on the boundary layer. The momentum addition region can be seen in figure 3. Boundary layer profiles extracted from these flows upstream of the plasma actuation are slightly fuller, due to entrainment effects of the momentum addition. Slightly downstream of the actuator, these velocity profiles become increasingly fuller as momentum is injected into the flow, especially in the near wall region of the boundary layer. Even farther downstream of the actuator, momentum added to the flow quickly diffuses out into the boundary layer, resulting in the velocity profiles with a more rounded shape. These changes in the velocity profiles can also be quantified using the shape factor of the boundary layer profiles along the length of the plate (figure 4(*d*)). The 'fullness' of the velocity profile is measured by its shape factor ($H = \frac{\delta^*}{\theta}$, where $\theta = \int_0^\infty (\frac{u}{u_\infty})(1 - \frac{u}{u_\infty})\,\mathrm{d}y$), where fuller velocity profiles have smaller values of the shape factor. The reduction in the shape factor from the baseline value of 2.6 indicates that the velocity profiles downstream of the plasma actuators are fuller than those with no actuation applied. Hence, based on the correlation between shape factor and flow stability developed by Wazzan *et al* [29], the flows with actuation should be more stable. Boundary layer heights around the plasma actuator are also modified due to the addition of momentum into the flow. It can be seen in figure 4(*a*) that increased momentum addition results in monotonically larger changes to the displacement boundary layer heights.

These exact baseflows have also been used in the examination of damping TS waves using DBD actuators [10].

3. Generation of boundary layer streaks

3.1. Bi-global stability approach

A bi-global stability approach is employed for studying the growth mechanisms of boundary layer streaks. This approach

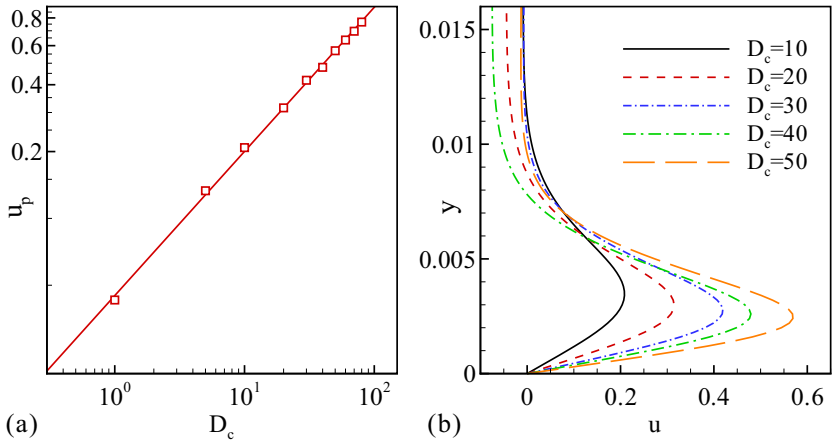

Figure 2. (*a*) Values of u_p used to calibrate D_c. (*b*) Velocity profiles at a location downstream of the plasma actuation for various values of D_c. From Riherd and Roy [10].

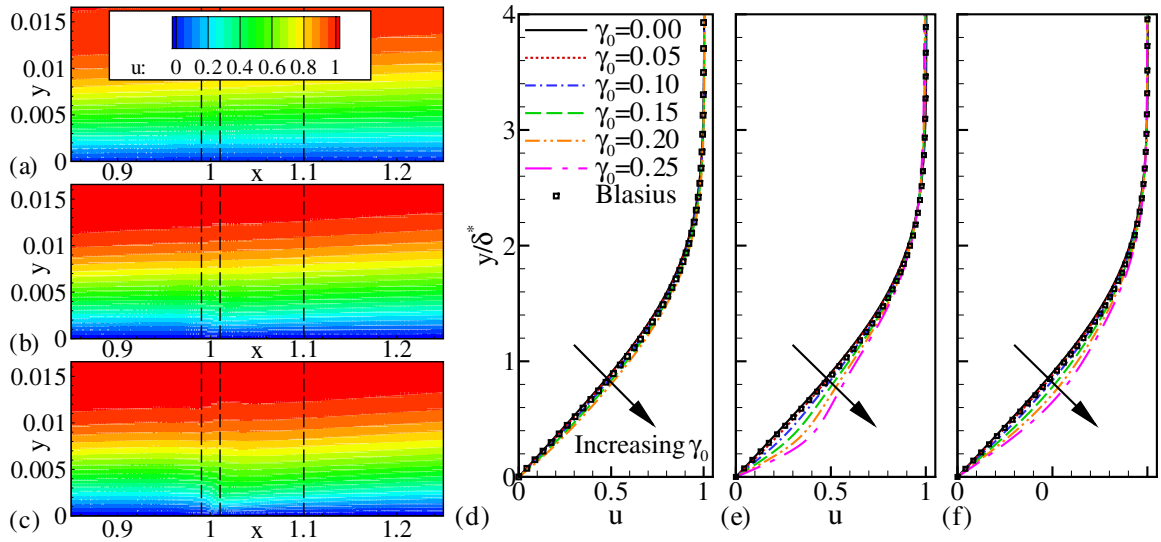

Figure 3. Velocity fields around the plasma actuator for the velocity ratios of (*a*) $\gamma_0 = 0.00$, (*b*) $\gamma_0 = 0.10$ and (*c*) $\gamma_0 = 0.20$. Boundary layer profiles at (*d*) $x = 0.99$, (*e*) $x = 1.01$ and (*f*) $x = 1.10$ are also shown. The dashed lines in (*a*)–(*c*) indicate locations where the boundary layer profiles are extracted from, and are shown in (*d*)–(*f*). From Riherd and Roy [10].

takes into account the effects of a two-dimensional, non-parallel flow, as well as the highly localized effects in the region where a body force is applied. The velocity field, u, and pressure field, p, can be decomposed into the steady equilibrium and perturbation components, where $u_i = \bar{u}_i + u_i'$ and $p = \bar{p} + p'$. Using this decomposition, the incompressible Navier–Stokes equations can be linearized around this steady point such that

$$\frac{\partial u_i'}{\partial x_i} = 0 \tag{2a}$$

$$\frac{\partial u_i'}{\partial t} + \bar{u}_j \frac{\partial u_i'}{\partial x_j} + u_j' \frac{\partial \bar{u}_i}{\partial x_j} + \frac{\partial p'}{\partial x_i} - \frac{1}{Re} \frac{\partial^2 u_i'}{\partial x_j^2} = 0. \tag{2b}$$

Assuming that these perturbations are periodic in time, such that $u_i' = \tilde{u}_i \exp(\mathrm{i}(\beta z - \omega t))$, the problem can be put into matrix operator form such that

$$\mathrm{i}\omega \boldsymbol{B}\boldsymbol{u} = \boldsymbol{A}\boldsymbol{u} + \boldsymbol{f} \tag{3}$$

where

$$\boldsymbol{u} = \begin{bmatrix} \tilde{u} \\ \tilde{v} \\ \tilde{w} \\ \tilde{p} \end{bmatrix}, \quad \boldsymbol{A} = \begin{bmatrix} \frac{\partial(\cdot)}{\partial x} & \frac{\partial(\cdot)}{\partial y} & \mathrm{i}\beta & 0 \\ \mathcal{C} - \mathcal{D} + \frac{\partial \bar{u}}{\partial x} & \frac{\partial \bar{u}}{\partial y} & 0 & \frac{\partial(\cdot)}{\partial x} \\ \frac{\partial \bar{v}}{\partial x} & \mathcal{C} - \mathcal{D} + \frac{\partial \bar{v}}{\partial y} & 0 & \frac{\partial(\cdot)}{\partial y} \\ 0 & 0 & \mathcal{C} - \mathcal{D} & \mathrm{i}\beta \end{bmatrix},$$

$$\boldsymbol{B} = \begin{bmatrix} 0 & 0 & 0 & 0 \\ I & 0 & 0 & 0 \\ 0 & I & 0 & 0 \\ 0 & 0 & I & 0 \end{bmatrix}. \tag{4}$$

The convection and viscous diffusion operators $\mathcal{C}$ and $\mathcal{D}$ are defined as $\mathcal{C} = \bar{u}\frac{\partial(\cdot)}{\partial x} + \bar{v}\frac{\partial(\cdot)}{\partial y}$ and $\mathcal{D} = \frac{1}{Re}(\frac{\partial^2(\cdot)}{\partial y^2} + \frac{\partial^2(\cdot)}{\partial y^2})$. $\boldsymbol{f}$ indicates a periodic forcing to the system. $\boldsymbol{u}$ represents the system's response to that force. Both $\boldsymbol{f}$ and $\boldsymbol{u}$ are complex vectors with real and imaginary parts. The response of the system can be evaluated by solving the system of equations shown above such that

$$\boldsymbol{u} = [\mathrm{i}\omega \boldsymbol{B} - \boldsymbol{A}]^{-1} \boldsymbol{f}. \tag{5}$$

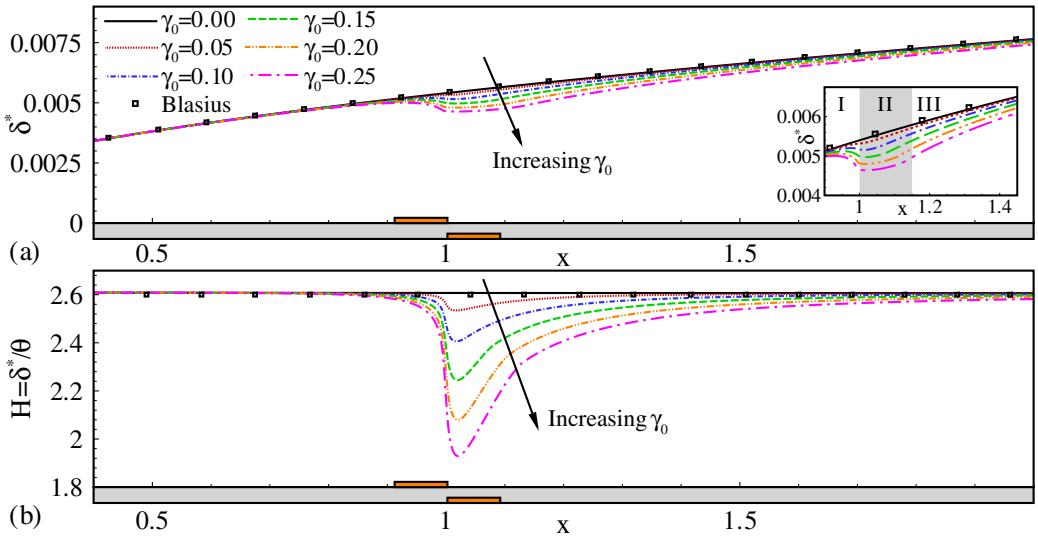

Figure 4. (*a*) δ^* and (*b*) the shape factor as a function of the velocity ratio, γ_0, for values ranging from 0 to 0.25, with a spacing of 0.05. The inset figure shows a zoomed in view near the actuator location with the three characteristic zones shown. The size of the actuator is exaggerated for better visibility. From Riherd and Roy [10].

For the present case the periodic forcing term $\boldsymbol{f}$ represents a non-homogeneous boundary condition at the inlet of the domain.

The benefits of this approach to the flow's stability are that wide parametric studies can be performed relatively easily. The linear growth of instabilities can be evaluated over a broad range of perturbations and frequencies. However, this comes at a cost. This model is unable to predict non-linear effects, such as the onset of turbulence. As such, the early stages of transition can be accurately portrayed using this approach, but the latter stages of transition and the potential energy savings due to the delay of transition should be evaluated using alternative methods, such as direct numerical simulations or wind tunnel experiments.

3.2. Numerical discretization and boundary conditions

In order to perform these calculations, the matrix operations described in equations (2*a*)–(4) are discretized on a semi-staggered mesh. The velocity fields and their gradients produced in section 2 were interpolated onto this mesh. The momentum equations are solved and velocity data is stored on a set of points coincident with the domain boundaries. The continuity equation is solved and pressure data is stored on the intermediate set of points. For the differencing, Chebyshev collocation methods are used in the y-direction. In the x-direction, fourth order accurate centred differencing is used for a majority of the domain. The exception to this is the streamwise convection term, $\bar{u}\frac{\partial(\cdot)}{\partial x}$. This term is up-winded using a third order accurate finite difference stencil. Next to the boundaries, lower order stencils are used.

At the inlet boundary, a set of perturbations are introduced, the downstream propagation of which is determined by solving the matrix inversion in equation (5). In order to evaluate the effects of boundary layer streaks, eigenmodes from a local, spatial stability analysis are introduced at the inlet. The resulting two-dimensional flow fields are used as to form a basis set from which the boundary layer streaks can be generated.

3.3. Boundary layer streak formation

Boundary layer streaks are non-normal, algebraically growing disturbances, and have been identified as the most amplified perturbation over finite lengths of time and distance. Typically, the most amplified perturbations are generated using a superposition of the eigenmodes of the system [30, 31], the computation of which is described in the previous subsection, such that

$$u' = \sum_i^{N_{\text{eig}}} c_i u_i' \tag{6a}$$

$$v' = \sum_i^{N_{\text{eig}}} c_i v_i' \tag{6b}$$

$$w' = \sum_i^{N_{\text{eig}}} c_i w_i'. \tag{6c}$$

In order to study the growth of these disturbances, a quantifying metric must be employed. The metric

$$G(x) = \frac{\mathcal{K}(x)}{\mathcal{K}_0} \tag{7}$$

is selected, as it describes the amplification of the perturbation's kinetic energy as it develops in the streamwise direction, where

$$\mathcal{K}_0 = \int_0^\infty \frac{1}{2}\left(u'^* u' + v'^* v' + w'^* w'\right) \mathrm{d}y \Big|_{x=\text{inlet}} \tag{8a}$$

$$\mathcal{K}(x) = \int_0^\infty \frac{1}{2}\left(u'^* u' + v'^* v' + w'^* w'\right) \mathrm{d}y \Big|_{x} \tag{8b}$$

Table 2. Details of the grid resolution study performed, as well as the number of eigenmodes used as a basis set for the optimal perturbations. The Fine-L, Fine-H, and Tall cases are identical.

Study	Case	N_x	N_y	L_x/δ_0^*	L_y/δ_0^*	$\Delta x/\delta_0^*$	$\Delta y_{\text{wall}}/\delta_0^*$	N_{eig}
Streamwise resolution	Coarse-L	513	65	1061.7	40	2.0736	0.024 09	64
	Medium-L	725	65	1061.7	40	1.4664	0.024 09	64
	Fine-L	1025	65	1061.7	40	1.0368	0.024 09	64
Wall normal resolution	Coarse-H	1025	33	1061.7	40	1.0368	0.096 31	32
	Medium-H	1025	49	1061.7	40	1.0368	0.042 82	48
	Fine-H	1025	65	1061.7	40	1.0368	0.024 09	64
Height	Short	1025	33	1061.7	20	1.0368	0.048 15	32
	Medium	1025	49	1061.7	30	1.0368	0.032 12	48
	Tall	1025	65	1061.7	40	1.0368	0.024 09	64

and * represents the complex conjugate. Furthermore, the most amplified perturbations are defined as those which maximize the growth in kinetic energy at some point along the streamwise direction, i.e.

$$G_{\max}(x) = \max_{\mathcal{K}_0 \neq 0} \frac{\mathcal{K}(x)}{\mathcal{K}_0}. \tag{9}$$

Farrell [30] describes finding the most amplified modes by forming a second eigenvalue problem,

$$\boldsymbol{K}_0^{-1}\boldsymbol{K}_x\boldsymbol{c} = \lambda\boldsymbol{c} \tag{10}$$

where $\boldsymbol{K}_0$ and $\boldsymbol{K}_x$ are mass matrices representing the modal products of the different eigenmodes at the inlet and at downstream locations such that

$$K_{0,ij} = \int_0^\infty \frac{1}{2}\left(u_i'^* u_j' + v_i'^* v_j' + w_i'^* w_j'\right) \mathrm{d}y\Big|_{x=\text{inlet}} \tag{11a}$$

$$K_{x,ij} = \int_0^\infty \frac{1}{2}\left(u_i'^* u_j' + v_i'^* v_j' + w_i'^* w_j'\right) \mathrm{d}y\Big|_{x} \tag{11b}$$

The largest eigenvalue (λ) of the problem described in equation (10) represents the amplification of the kinetic energy at a downstream point ($G_{\max}(x)$, equation (9)). The initial conditions at the inlet can be extracted by the linear superposition of eigenvalue perturbations described in equation (6) by the coefficents given in the associated eigenvector, $\boldsymbol{c}$.

3.4. Grid resolution studies

A grid resolution study has been performed in order to ensure that the problem is adequately resolved. The details of the domain and mesh parameters are indicated in table 2. This study has been performed primarily on the unforced boundary layer, but addition grid resolution studies for boundary layers where momentum addition was applied were also performed, indicating similar convergence.

For the grid resolution study, perturbations with spanwise wave numbers of $\beta = 0.45$, 0.60 and 0.75 and a temporal frequency of $\omega = 0$ are examined. The maximum amplification of perturbations at streamwise location of $x/\delta_0^* = 600$ is considered. It can be seen in figures 5(a) and (b), that the streamwise resolutions chosen converge very well in the absence of momentum injection in the boundary layer. Furthermore, the wall normal grid resolution appears to be sufficient (figure 5(c)). A study of the domain height also shows convergence of the perturbation's magnitude (figure 5(d)).

A case with a body force applied to the boundary layer is also considered. The streamwise resolution in the near actuator region may present itself as difficult to resolve due to the steep gradients in the streamwise direction. However, based on the grid resolution study performed (figure 6), the Fine-L mesh sufficiently resolves all of the important effects in the flow.

4. Damping of boundary layer streaks

4.1. Baseline case

Beginning with the unforced boundary layer, several things should be noted about the streaks that are generated using this method. First, the most amplified boundary layer streaks display similar trends in growth and structure regardless of where the optimization is performed in the streamwise direction, but there are quantitative variations in the growth depending on where along the streamwise direction the optimization takes place (figure 7(a)). The growth of these streaks is driven by streamwise oriented vortices in the boundary layer (figure 7(b)). These streaks start off as having a small, if not negligible streamwise velocity component. However, the streamwise oriented vortices transfer low momentum fluid upwards and away from the surface of the boundary layer on one side of the vortex, while simultaneously transporting high momentum fluid from the free stream downwards closer to the surface on the other. This results in localized high and low speed streaks in the surface (figure 7(c)). As this process occurs, the magnitude of the streak grows as the vorticity continues to transport streamwise momentum into and out of the boundary layer, but after a certain length of boundary layer, viscous effects dissipate the streamwise vorticity, which limit the maximum growth, as well as the boundary layer streaks, which leads to their eventual decay in the absence of non-linear effects. This process is very well documented in the literature for both one-dimensional [31, 32] and two-dimensional flows [33, 34]. The maximum level of growth for this type of perturbation is very strongly tied to the spanwise wavenumber of the perturbation, and wider perturbations grow more slowly at first, but ultimately reach larger magnitudes, but at points much farther downstream of narrower perturbations.

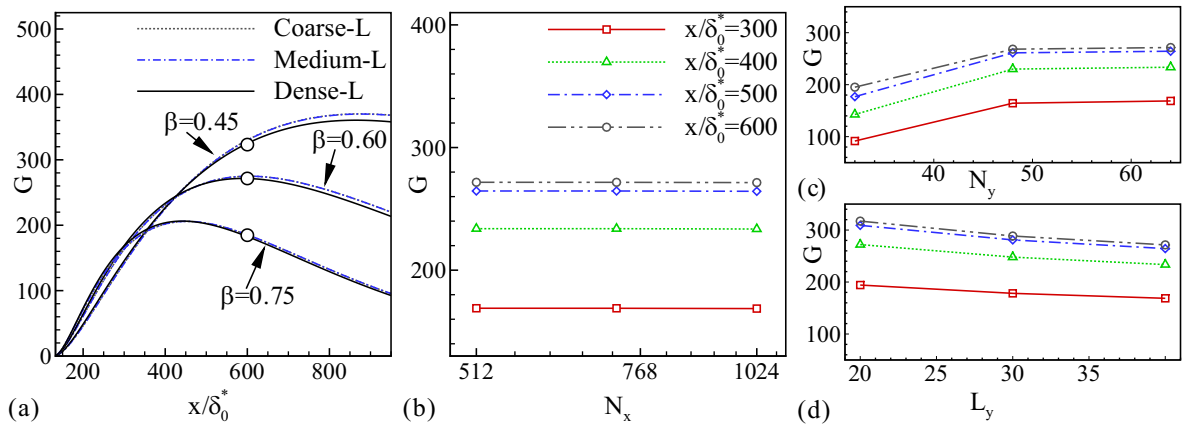

Figure 5. (*a*) Kinetic energy amplification for perturbations of spanwise wavenumber $\beta = 0.45, 0.60, 0.75$ that are most amplified at the location $x/\delta_0^* = 600$ as a function of the streamwise resolution, along with (*b*) data collected at individual points along the streamwise direction for the $\beta = 0.60$ case. Convergence data for the (*c*) wall normal resolution and (*d*) domain height are also shown.

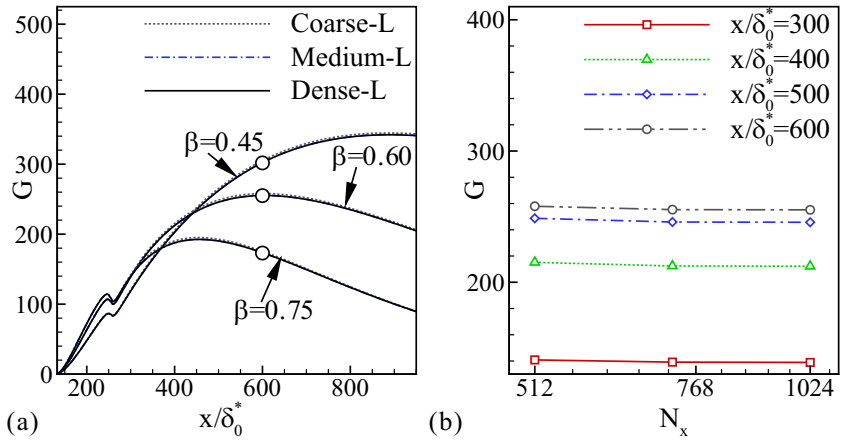

Figure 6. (*a*) Kinetic energy amplification for perturbations of spanwise wavenumber $\beta = 0.45, 0.60, 0.75$ that are most amplified at the location $x/\delta_0^* = 600$ case where body force is injected ($\gamma_0 = 0.20$) in the boundary layer as a function of the streamwise resolution, along with (*b*) data collected at individual points along the streamwise direction for the $\beta = 0.60$.

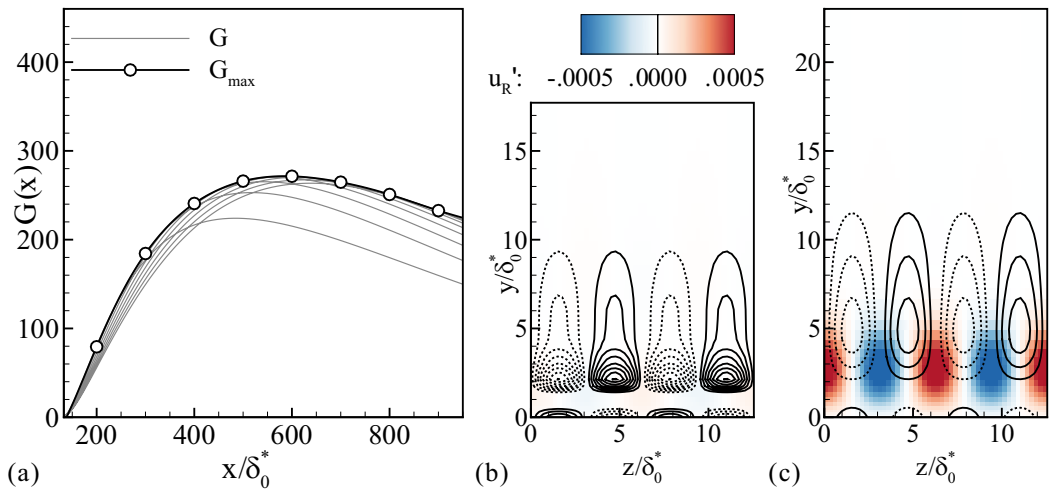

Figure 7. (*a*) Growth of kinetic energy contained in boundary layer streaks for $\beta = 0.6$ (thin lines) as a function of where the most amplified perturbation is determined (circles). The thick line represents the envelope of maximum growth as a function of the streamwise location for $\beta = 0.6$. (*b*) Spanwise slices of the flow field at the initial condition and (*c*) flow at $x/\delta_0^* = 600$ are shown for the most amplified perturbation at $x/\delta_0^* = 600$ for $\beta = 0.6$. The contour lines indicate the streamwise vorticity, while the shading indicates the streamwise velocity.

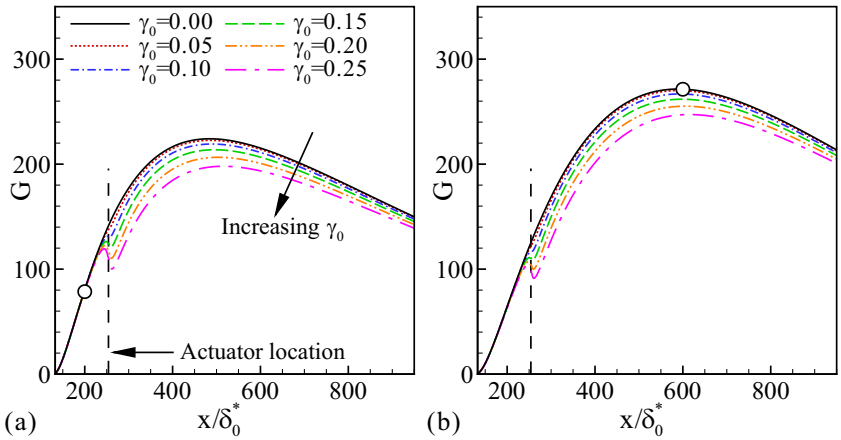

Figure 8. Growth of kinetic energy contained in boundary layer streaks for $\beta = 0.6$ with and without plasma actuation. The streaks shown are the most amplified perturbations at (*a*) $x/\delta_0^* = 200$ and (*b*) $x/\delta_0^* = 600$. The dashed vertical line indicates the location of the plasma actuator, and the circle indicates where this perturbation is the most amplified perturbation, as well as $G_{\max}$ for the unforced case.

4.2. With plasma actuation

When a plasma-based body force is applied to the flow, adding momentum into the boundary layer, it appears that the boundary layer streaks are reduced in amplitude. Figure 8 shows that damping of the streaks downstream of the body force can occur, regardless of where they are considered to be the most amplified streak. Furthermore, depending on the magnitude of the body force and where the streak amplitude is considered, this damping appears be up to 20% of the overall streak magnitude.

Having observed that the kinetic energy contained in these streaks is reduced downstream of the plasma actuation, the next item of concern is to determine why this damping occurs. In order to identify the source of this damping, a Reynolds-averaged Navier–Stokes (RANS) based kinetic energy balance for these perturbations can be used.

$$\frac{D\left(TKE'\right)}{Dt} + \frac{\partial T_i}{\partial x_i} = P - \epsilon, \tag{12}$$

where

$$TKE' = \frac{1}{2}\left(\overline{u_i'^* u_i'}\right) \tag{13a}$$

$$P = -\overline{u_i'^* u_j'}\frac{\partial \bar{u}_i}{\partial x_j} \tag{13b}$$

$$\epsilon = \frac{2}{Re}\left(\overline{s_{ij}'^* s_{ij}'}\right) \tag{13c}$$

and $\frac{\partial T_i}{\partial x_i}$ represent accelerative transport terms due to the perturbation's own pressure and strain fluctuations. The right-hand side terms in equation (12), P and ϵ, represent the production and dissipation of kinetic energy in the perturbation, respectively.

Evaluating the perturbation kinetic energy, production, and dissipation terms (figure 9), it becomes apparent that the addition of a body force region in the boundary layer interferes with the production of the perturbation's kinetic energy. Inside of the body force region, it appears that not only is the production of kinetic energy attenuated, but if the amount of body force is high enough, it can even become negative. Examining the effects of viscous dissipation, it appears that this sink for the perturbation's energy is largely unaffected by the addition of plasma actuation, though there are some variations due to the decreased magnitude of the perturbation.

Decomposing the production of kinetic energy into its individual terms, the localized effects become even more apparent (figure 10). The effects of the $\overline{v'u'}\frac{\partial \bar{v}}{\partial x}$ and $\overline{v'u'}\frac{\partial \bar{v}}{\partial x}$ on the energy production are negligible with or without the body force added to the flow, but the changes to the $\overline{u'u'}\frac{\partial \bar{u}}{\partial x}$ and $\overline{u'v'}\frac{\partial \bar{u}}{\partial y}$ terms and the changes to them are significant. It appears that the majority of the negative production in the body force region is due to the $\overline{u'u'}\frac{\partial \bar{u}}{\partial x}$ term. This term, which is the less dominant production term in the unforced boundary layer, is reliant on the streamwise development of the flow. As the addition of a very localized body force generates significant high gradients in the streamwise direction, it logically follows that this production term would be affected. As the flow is accelerated by the co-flow actuation, the velocity gradient $\frac{\partial \bar{u}}{\partial x}$ increases in magnitude, leading to a reduction in the perturbation's kinetic energy production by the $\overline{u'u'}\frac{\partial \bar{u}}{\partial x}$ term. The other term of significance is the $\overline{u'v'}\frac{\partial \bar{u}}{\partial y}$ term, which is responsible for a majority of the energy production. This term also shows a very localized attenuation in production, as well as a slight decreased in production downstream of the actuator. However, this effect does not seem to be as dominant to reducing the streak magnitude as the $\overline{u'u'}\frac{\partial \bar{u}}{\partial x}$ term.

The change in perturbation kinetic energy production has also been noted in the stabilization of the TS wave [10]. However in that scenario, the stabilization is primarily due to modification of the $\overline{u'v'}\frac{\partial \bar{u}}{\partial y}$ term, though local stabilization due to the $\overline{u'u'}\frac{\partial \bar{u}}{\partial x}$ term also plays a small part. For the TS wave, the streamwise and wall normal velocity components are of comparable magnitude. However, for boundary layer streaks, the streamwise velocity component is far greater in magnitude, and a large difference in magnitude of the $\overline{u'u'}$ and $\overline{u'v'}$ terms reflects this. As such, for boundary layer streaks, changes to $\frac{\partial \bar{u}}{\partial x}$ will have a greater impact on the production term than $\frac{\partial \bar{u}}{\partial y}$. Therefore, the localized acceleration of the flow by the co-flow oriented body force is stabilizing, but only in the

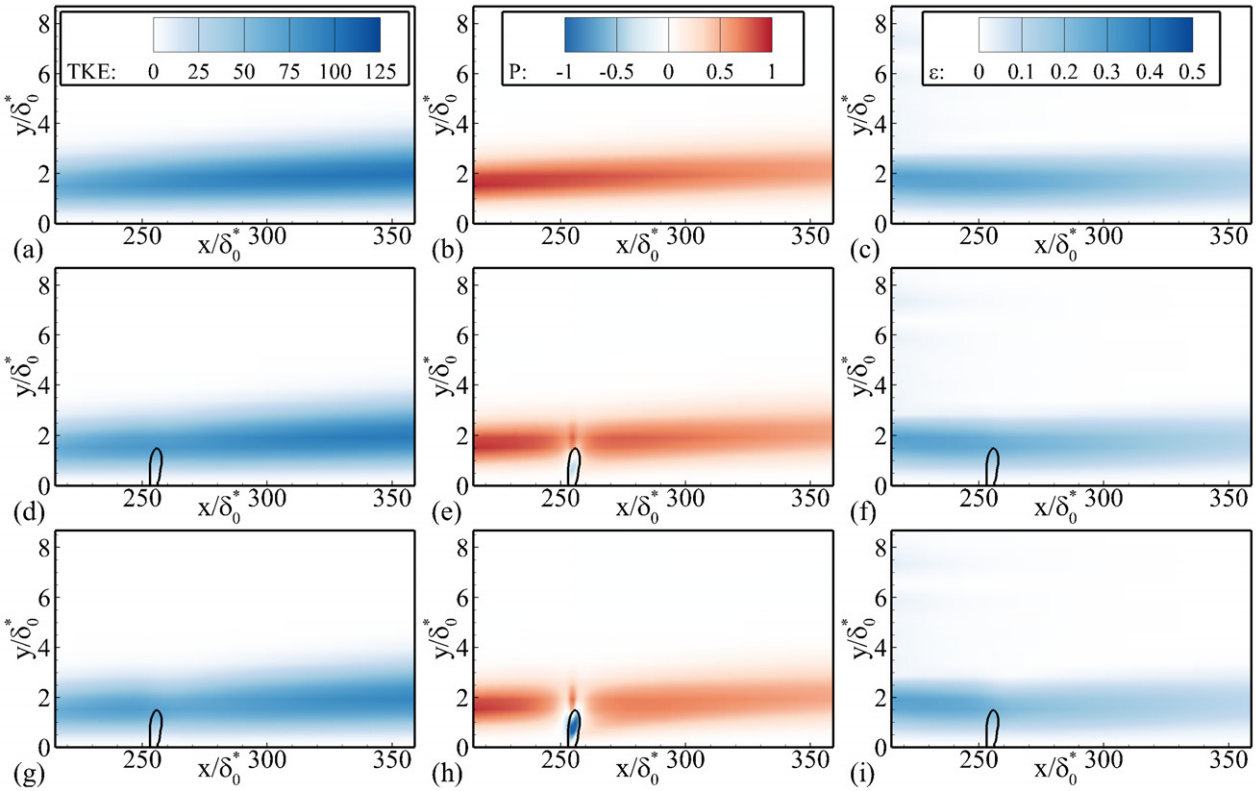

Figure 9. (a), (d), (g) Turbulent kinetic energy, (b), $(e$, (h) kinetic energy production, and (c), (f), (i) kinetic energy dissipation of boundary layer streaks for the (a)–(c) unforced, (d)–(f) $\gamma_0 = 0.10$ and (g)–(i) $\gamma_0 = 0.20$ cases, for the most amplified perturbation at $x/\delta_0^* = 200$.

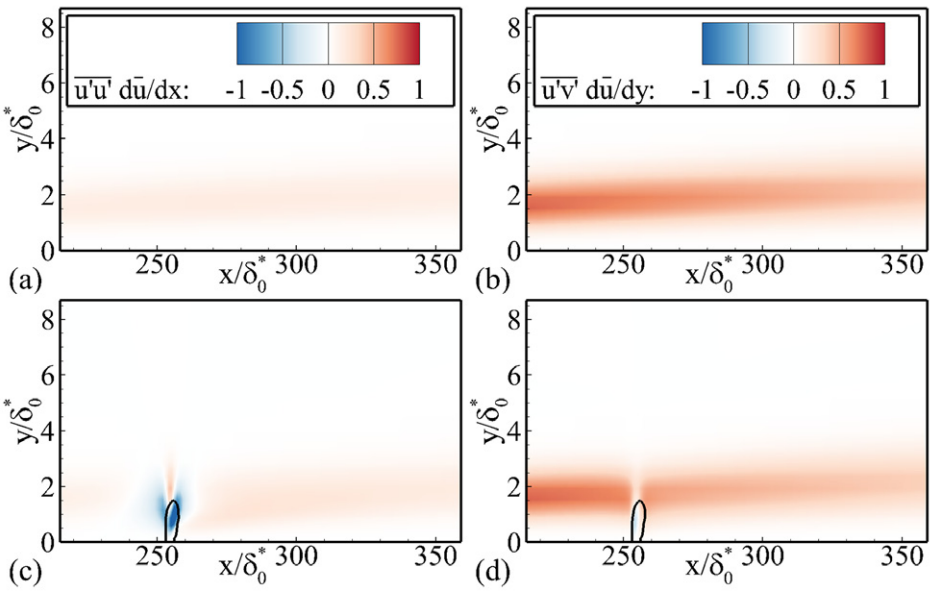

Figure 10. Comparison of the two dominant perturbation kinetic energy production terms (a), (b) without and (c), (d) with plasma actuation $(\gamma_0 = 0.20)$.

region immediately around the plasma actuator. Downstream of the actuator, these effects reverse as the flow relaxes back to a zero pressure gradient boundary layer, and the normalized production due to the $\overline{u'u'}\frac{\partial \bar{u}}{\partial x}$ term will be increased relative to the baseline flow. This offsets most of the stabilization due to the fuller downstream boundary layer profile. Even so, the localized stabilization effects are sufficient enough to ensure a reduced magnitude of the streak in the downstream region. The extend of these stabilizing effects can be seen more clearly in figure 11.

4.3. Scaling of the damping

The observation that the addition of a plasma-based body force can reduce the amplitude of boundary layer streaks is interesting and suggests that there is potential in this application, but it

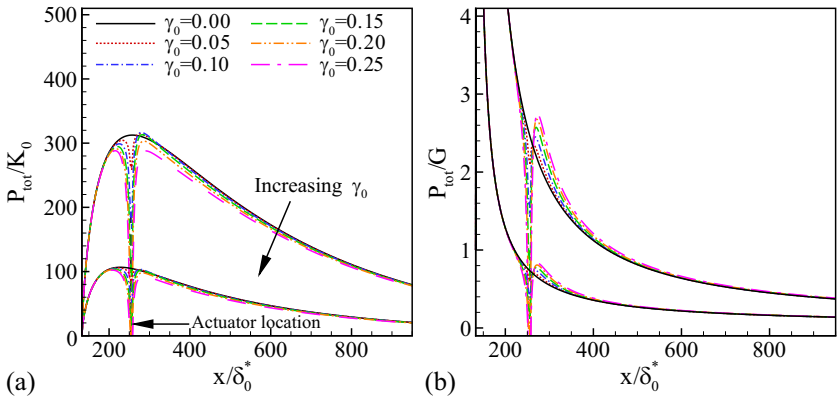

Figure 11. (*a*) Total production of kinetic energy in the boundary layer ($P_{\text{tot}}(x) = \int_{y=0}^{\infty} P(x, y)\,\mathrm{d}y$) for varying levels of plasma actuation. This data is also presented once normalized by the total kinetic energy contained in the perturbation ($\mathcal{K}(x)$).

would be very beneficial to characterize the behaviour of these devices over a broad range of parameters, as well as to reduce the scaling effects down to a single value for comparison.

Parametric studies have been performed determining the value of $G_{\max}$ as a function of the spanwise wavenumber, as well as the velocity ratio along the streamwise direction (figure 12). This approach, while it does not focus on the growth and decay of individual streaks, does provide information about what the maximum possible growth will be. As such, this approach describes the growth of the most amplified perturbation with or without the effects of the plasma actuator.

In figure 12(*a*), the values of $G_{\max}$ are shown across a spectrum of spanwise wavenumbers for the unforced boundary layer, indicating that wider perturbations (lower β) grow more slowly initially, but eventually grow to larger magnitudes. With the addition of plasma control ($\gamma_0 = 0.20$, figure 12(*b*)), this trend continues to hold, but there is a noticeable dip in the perturbation's energy located around the plasma actuator for all of the wavenumbers examined. Further examining this data, the maximum of $G_{\max}$ for all of the wavenumbers examined is shown in figure 12(*c*). It can be seen in that figure that the addition of the body force damps the the entire envelope of most amplified potential perturbations.

In order to quantify the damping of these perturbations, the metric

$$H_{\max} = \frac{G_{\max}(x, \beta, \gamma_0)}{G_{\max}(x, \beta, \gamma_0 = 0)} \tag{14}$$

is used, which compares the ratio of the maximum disturbance amplification with and without plasma actuation. Evaluating this metric at a point downstream of the plasma actuator ($x/\delta_0^* = 300$), it can be seen that there is damping of the perturbations, and that this damping can be significant, up to 25% of the overall magnitude of the perturbation, depending on the magnitude of the plasma actuation is examined. While the amplification of these perturbations is obviously wavenumber dependent (figure 13(*a*)), the damping effects are not as sensitive to the spanwise wavenumber (figure 13(*b*)). It would appear that while there is a slight spanwise wavenumber dependence, the damping is much more strongly dependent on the magnitude of the plasma actuation.

Comparing the damping of the streaks across a the velocity ratio and total amount of body force added to the flow (which is proportional to the parameter D_c), several trends become apparent. The magnitude of the damping increases monotonically with respect to both parameters. While the damping is very low (≈5%) for the weaker levels of plasma actuation ($\gamma_0 < 0.1$), once the plasma actuation reaches a high enough level, a linear trend in the damping appears with respect to the total amount of body force added to the flow. As such, it follows that the damping follows a power law trend for the velocity ratio as u_p is proportional to D_c. However, when compared to the power added to the flow by the plasma body force (figure 14(*c*)), the monotonicity of the response continues, but there is a decreasing margin of gain as additional power is added. However, this is complicated by the fact that the power supplied to the plasma actuator does not all go to the body force and that plasma actuators become more efficient as they are operated at higher voltages (i.e. greater body forces) [35].

5. Conclusions

Using a bi-global stability analysis, it has been shown that DBD plasma actuators may be used to stabilize boundary layer streaks, filling a gap in the understanding of how these actuators can be used to delay the onset of turbulent flow in boundary layers with respect to algebraic and by-pass transition scenarios. The physical mechanisms responsible for flow stabilization have been examined using a RANS approach to the perturbation growth. Parametric studies examining these streaks over a range of wavenumbers and levels of plasma actuation have also been performed. The damping of these streaks is predicted to be on the order of 5–25% of the total streak magnitude, and occurs over the entire range of spanwise wavenumbers examined.

The stabilization of these streaks can be attributed to highly localized effects around the plasma induced body force. The addition of the body force locally deforms the flow field. In turn, the localized variations in the flow field attenuate the linearized production of the streak's kinetic energy, and for sufficiently high levels of actuation, these flow field variations can induce negative kinetic energy production.

Based on the parametric studies performed, the overall effect of stabilization scales linearly with the magnitude of the

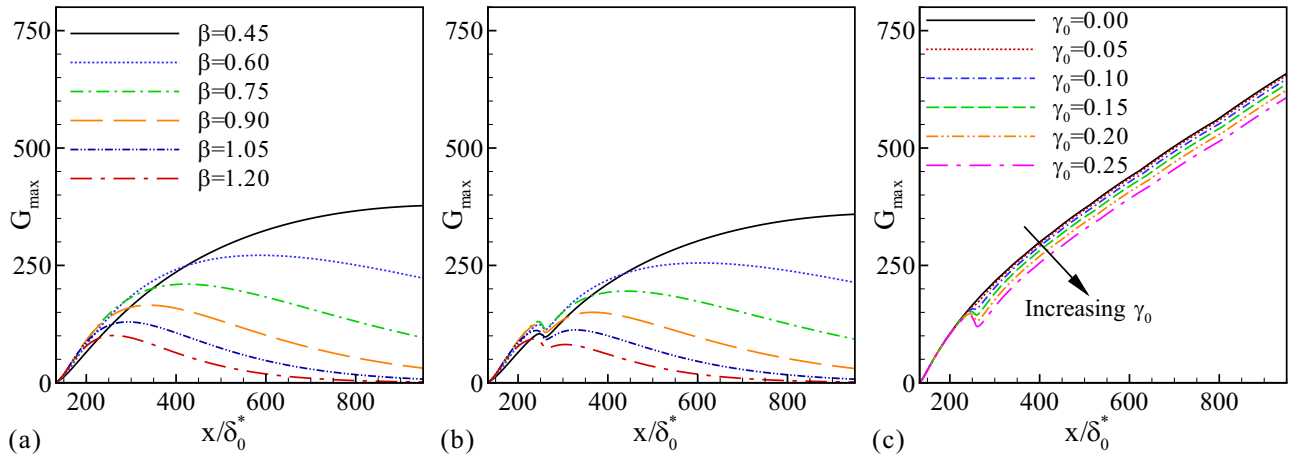

Figure 12. Amplitude of the most amplified perturbations (G_{max}) (*a*) without and (*b*) with ($\gamma_0 = 0.2$) a plasma actuator as a function of the spanwise wavenumber and location. (*c*) The maximum of G_{max} taken over all of the spanwise wavenumbers examined for varying levels of plasma actuation.

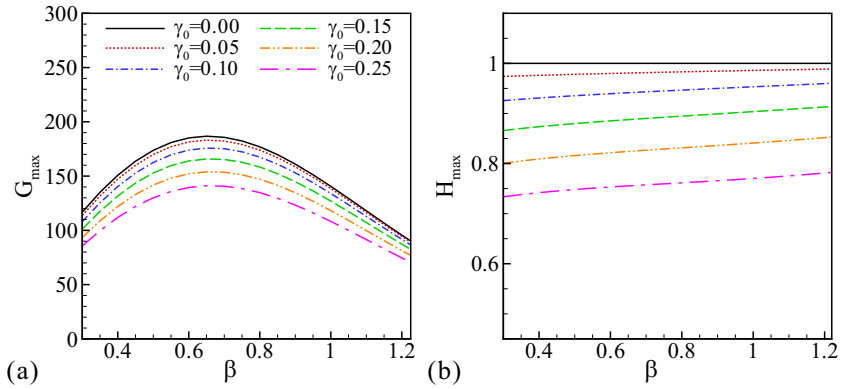

Figure 13. (*a*) G_{max} and (*b*) H_{max} at the location $x/\delta_0^* = 300$ as a function of the spanwise wavenumber and the magnitude of the plasma actuation.

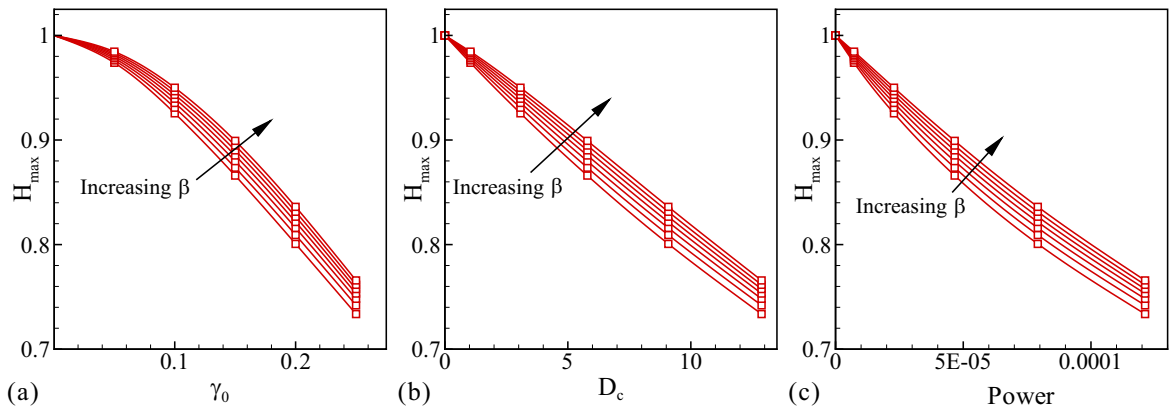

Figure 14. H_{max} in terms of the (*a*) wall jet velocity ratio, (*b*) body force magnitude applied to the flow, and (*c*) power applied to the base flow over the domain in figure 1 (Power $= \int D_c(f_x u + f_y v)\,\mathrm{d}x\,\mathrm{d}y$). H_{max} is shown for spanwise wavenumbers, β, between 0.3 and 0.9.

body force applied to the flow by the plasma actuators. There is some wavenumber dependence to the stabilization, but the attenuation of the streaky structures in the flow is more strongly tied to the magnitude of the plasma actuation.

Furthermore, this analysis (along with prior studies on stabilizing the TS wave) indicates that DBD actuators used in a continuous manner are able to suppress a broader range of perturbations that occur over multiple paths to transition than have been previously examined. While the damping of boundary layer streaks is not as dramatic as the damping of TS waves, the present analysis indicates that the stabilization of boundary layer streaks by DBD actuators can be significant, and indicates that these actuators are not limited to a stabilizing a single path to transition.

As this type of actuators continues to mature, future studies should focus examining how well these actuators scale

up at higher Reynolds numbers and under more realistic disturbance environments, particularly conditions that will be experienced during operation of air and ground vehicles. Should the effectiveness of these actuators still hold under more rigorous conditions, it would indicate that these devices have potential to reduce turbulent skin friction drag for more and more applications.

The present study has taken a linear approach to examine a broad parameter set, at the expense of non-linear effects, such as the onset of turbulence in the flow. However, the effect of transition delay in terms of the power savings and the power required to operate the plasma actuator should be evaluated as part of future efforts, and comparisons should be made with other methods of active and passive flow stabilization (i.e. boundary layer suction, riblets, etc). Direct measurements of the power usage and savings will either show that this approach is too inefficient to be of use or bolster the case for plasma actuators as a tool to stabilize boundary layers.

Acknowledgments

The authors would like to thank Dr Miguel Visbal of the Air Force Research Laboratory for the use of the code FDL3DI. The first author would also like to thank the University of Florida's Graduate School Fellowship Award, which provided partial support for this study.

References

[1] Corke T C, Enloe C L and Wilkinson S P 2010 Dielectric barrier discharge plasma actuators for flow control *Ann. Rev. Fluid Mech.* **66** 505–29
[2] Moreau E 2007 Airflow control by non-thermal plasma actuators *J. Phys. D: Appl. Phys.* **40** 605–36
[3] Wang J-J, Choi K-S, Feng L-H, Jukes T N and Whalley R D 2013 Recent developments in DBD plasma flow control *Prog. Aerospace Sci.* **62** 52–78
[4] Grundmann S and Tropea C 2008 Active cancellation of artificially induced Tollmien–Schlichting waves using plasma actuators *Exp. Fluids* **44** 795–806
[5] Grundmann S and Tropea C 2008 Delay of boundary-layer transition using plasma actuators *46th AIAA Aerospace Sciences Meeting (Reno, NV, 2008) AIAA Paper AIAA 2008-1369*
[6] Grundmann S and Tropea C 2009 Experimental damping of boundary-layer oscillations using DBD plasma actuators *Int. J. Heat Fluid Flow* **30** 394–402
[7] Duchmann A, Kurz A, Widmann A, Grundmann S and Tropea C 2012 Characterization of Tollmien–Schlichting wave damping by DBD plasma actuators using phase-locked PIV *50th AIAA Aerospace Sciences Meeting (Nashville, TN, 2012) AIAA Paper AIAA-2012-0903*
[8] Duchmann A, Grundmann S and Tropea C 2013 Delay of natural transition with dielectric barrier discharges *Exp. Fluids* **54** 1–12
[9] Riherd M, Roy S and Balachandar S 2014 Local stability effects of plasma actuation on a zero pressure gradient boundary layer *Theor. Computat. Fluid Dyn.* **28** 65–87
[10] Riherd M and Roy S 2013 Damping Tollmien–Schlichting waves in a boundary layer using plasma actuators *J. Phys. D: Appl. Phys.* **46** 485203
[11] Morkovin M V 1969 On the many faces of transition *Viscous Drag Reduction* (New York: Plenum) pp 1–31
[12] Tumin A and Reshotko E 2001 Spatial theory of optimal disturbances in boundary layers *Phys. Fluids* **13** 2097–104
[13] Reshotko E 2001 Transient growth: a factor in bypass transition *Phys. Fluids* **13** 1067–75
[14] Brandt L, Schlatter P and Henningson D S 2004 Transition in boundary layers subject to free-stream turbulence *J. Fluid Mech.* **517** 167–98
[15] Zaki T A and Durbin P A 2006 Continuous mode transition and the effects of pressure gradient *J. Fluid Mech.* **563** 357–88
[16] Hanson R E, Lavoie P, Naguib A M and Morrison J F 2010 Control of transient growth induced boundary layer control using plasma actuators *7th IUTAM Symp. on Laminar-Turbulent Transition (Stockholm)*
[17] Hanson R E, Lavoie P, Naguib A M and Morrison J F 2010 Transient growth instability cancelation by a plasma actuator array *Exp. Fluids* **49** 1339–48
[18] Fransson J H M, Brandt L, Talamelli A and Cossu C 2005 Experimental study of the stabilization of Tollmien–Schlichting waves by finite amplitude streaks *Phys. Fluids* **17** 054110
[19] Fransson J H M, Talamelli A, Brandt L and Cossu C 2006 Delaying transition to turbulence by a passive mechanism *Phys. Rev. Lett.* **96** 064501
[20] Andersson P, Brandt L, Bottaro A and Henningson D S 2001 On the breakdown of boundary layer streaks *J. Fluid Mech.* **428** 29–60
[21] Hœpffner J, Brandt L and Henningson D S 2005 Transient growth on boundary layer streaks *J. Fluid Mech.* **537** 91–100
[22] Joslin R D 1998 Aircraft laminar flow control *Ann. Rev. Fluid Mech.* **30** 1–29
[23] Cathalifaud P and Luchini P 2000 Algebraic growth in boundary layers: optimal control by blowing and suction at the wall *Eur. J. Mech.* B **19** 469–90
[24] Grek G R, Kozlov V V and Titarenko S V 1996 An experimental study of the influence of riblets on transition *J. Fluid Mech.* **315** 31–49
[25] Klumpp S, Meinke M and der W S 2010 Numerical simulation of riblet controlled spatial transition in a zero-pressure-gradient boundary layer *Flow, Turbul. Combust.* **85** 57–71
[26] Rizzeta D P, Visbal M R and Morgan P E 2008 A high-order compact finite-difference scheme for large-eddy simulations of active flow control *Prog. Aerospace Sci.* **44** 397–426
[27] Singh K P and Roy S 2008 Force approximation for a plasma actuator operating in atmospheric air *J. Appl. Phys.* **103** 013305
[28] Durscher R and Roy S 2012 Evaluation of thrust measurement techniques for dielectric barrier discharge actuators *Exp. Fluids* 1165–76
[29] Wazzan A R, Gazley C and Smith A M O 1979 Tollmien–Schlichting waves and Transition: heated and adiabatic wedge flows with applications to bodies of revolution *Prog. Aerospace Sci.* **18** 351–92
[30] Farrell B F 1988 Optimal excitation of perturbations in viscous shear flow *Phys. Fluids* **31** 2093–2102
[31] Butler K M and Farrell B F 1992 Three-dimensional optimal perturbations in viscous shear flow *Phys. Fluids* A **4** 1637–50
[32] Landahl M T 1980 A note on an algebraic instability of invisic parallel shear flows *J. Fluid Mech.* **98** 243–51
[33] Luchini P 2000 Reynolds-number-independent instability of the boundary layer over a flat surface: optimal perturbations *J. Fluid Mech.* **404** 289–309
[34] White E B 2002 Transient growth of stationary disturbances in a flat plate boundary layer *Phys. Fluids* **14** 4429
[35] Kriegseis J, Duchmann A, Tropea C and Grundmann S 2013 On the classification of dielectric barrier discharge plasma actuators: a comprehensive performance evaluation study *J. Appl. Phys.* **114** 053301